

Imaging the Thermalization of Hot Carriers After Thermionic Emission Over a Polytype Barrier

Fabian Könemann¹, I-Ju Chen,² Sebastian Lehmann,² Claes Thelander,² and Bernd Gotsmann^{1,*}

¹IBM Research – Zurich, Säumerstrasse 4, 8803 Rüschlikon, Switzerland

²Solid State Physics and NanoLund, Lund University, S-221 00 Lund, Sweden



(Received 28 November 2019; revised manuscript received 13 December 2019; accepted 17 March 2020; published 15 May 2020)

The thermalization of nonequilibrium charge carriers is at the heart of thermoelectric energy conversion. In nanoscale systems, the equilibration length can be on the order of the system size, leading to a situation where thermoelectric effects need to be considered as spatially distributed, rather than localized at junctions. The energy exchange between charge carriers and phonons is of fundamental scientific and technological interest, but their assessment poses significant experimental challenges. We address these challenges by imaging the temperature change induced by Peltier effects in crystal phase engineered InAs nanowire (NW) devices. Using high-resolution scanning thermal microscopy (SThM), we study current-carrying InAs NWs, which feature a barrier segment of wurtzite (WZ) of varying length in a NW of otherwise zincblende (ZB) crystal phase. The energy barrier acts as a filter for electron transport around the Fermi energy, giving rise to a thermoelectric effect. We find that thermalization through electron-phonon heat exchange extends over the entire device. We analyze the temperature profile along a nanowire by comparing it to spatially dependent heat diffusion and electron thermalization models. We are able to extract the governing properties of the system, including the electron thermalization length of 223 ± 9 nm, Peltier coefficient and Seebeck coefficient introduced by the barrier of 39 ± 7 mV and 89 ± 21 $\mu\text{V/K}$, respectively, and a thermal conductivity along the wire axis of 8.9 ± 0.5 W/m K. Finally, we compare two ways to extract the elusive thermal boundary conductance between the NW and underlying substrate.

DOI: 10.1103/PhysRevApplied.13.054035

I. INTRODUCTION

Thermoelectric effects, such as Peltier and Seebeck effects, have been explored for solid-state cooling and energy harvesting devices, respectively. However, the low intrinsic thermoelectric efficiency has been hampering a wide use of these effects in technology [1]. One of the popular approaches to increase efficiency is to exploit energy filtering of charge carriers passing an energy barrier, an effect often referred to as thermionic emission [2–6]. It is not straightforward to exploit this effect due to difficulties in creating high-quality (ideally atomically defined) interfaces between a reservoir material (semiconductor or metal) and a barrier region, and to control the chemical potential across such heterostructures. The heterostructure between the wurtzite (WZ) and zincblende (ZB) crystal phase in InAs nanowires (NWs) are an interesting candidate for thermionic emission structures. In InAs and most other III-V NWs the crystal phase can be controlled during growth [7–10], and interfaces between the two phases are inherently atomically sharp. Such InAs NW crystal

phase heterostructures have recently been studied in their transport properties, and it was found that the WZ phase has a positive conduction band offset by about 135 meV compared to the ZB phase [11,12]. This property has successfully been exploited for creating quantum dot devices [13–15].

The study of thermoelectric effects in nanostructures is of relevance beyond energy conversion applications. With increasing miniaturization of electronic devices, thermoelectric effects have become important for operation in, for example, resistive [16,17] and phase-change [18,19] memory devices or transistors [20], influencing power consumption and device failure. One of the scientific questions around such applications is related to the length scale over which thermalization occurs. In thermoelectric structures and devices on the macroscale, the generation of Peltier heat can safely be assumed to occur sharply at the interface between two materials. The equilibration of charge carriers passing a barrier, however, can be on the order of a hundred nanometers and is therefore comparable or even larger than device dimensions. Therefore, on the nanoscale, the simplified picture of thermoelectricity must be refined. However, measurement techniques to

*bgo@zurich.ibm.com

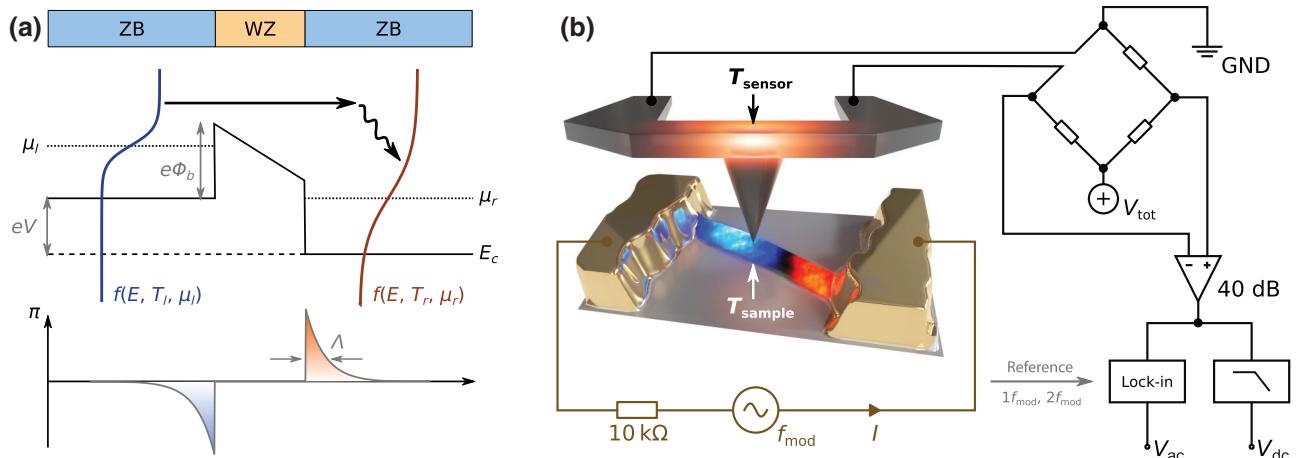


FIG. 1. (a) Schematic representation of the thermionic emission effect that leads to Peltier heating and cooling. The conduction band energy E_c has a positive offset $e\Phi_b$ in the WZ segment with respect to the surrounding ZB material. This gives rise to an energy barrier that acts as a filter for conduction electrons around the Fermi energy μ . When a bias V is applied across the WZ segment, such that the Fermi energy μ_l on the left is higher with respect to the Fermi energy μ_r on the right, only “hot” electrons from the high-energy tail of the left-side Fermi distribution can be emitted over the barrier and contribute to electrical conduction. They thermalize on the right side by scattering with a characteristic thermalization length Λ , widening the electron and phonon distributions and thereby increasing the temperature on the right side. At the same time, the distributions on the left side are narrowed, meaning that the temperature decreases there. An approximately exponentially distributed heating and cooling power arises at the junctions. The electronic current density therefore does not only transport charge, but also heat across the barrier. (b) Schematic representation of the measurement technique. V_{tot} is the total dc bias applied across the Wheatstone bridge relative to ground (GND).

probe thermalization have not been available. Thermal and thermoelectric effects in NWs and other nanostructures are generally difficult to quantify [21].

Here we apply an imaging technique to measure the temperature distribution of a thermoelectric nanowire device operando. Using scanning thermal microscopy, we obtain such images with a resolution of at least 10 nm [22–24]. The method has recently been used to study geometrically enhanced Peltier effects at a graphene constriction [25]. From the resulting temperature maps, we can extract thermal properties such as the thermal conductivity and the Peltier coefficient, and, importantly, the equilibration length of the charge carriers and a related density of Peltier heat production [5,26,27]. Note that in this paper, we use the term Peltier effect to refer both to heat pumping in response to an electrical current by thermionic emission over the barrier, and to heat pumping in response to an electrical current at the semiconductor-metal interfaces at the contacts.

The sample system chosen here is InAs NWs of ZB phase with a WZ segment length of 40 to 160 nm; see Fig. 1(a). The nanowires are placed on an n -doped Si substrate covered by 200 nm SiO_2 and contacted using nickel-gold metal contacts [Fig. 1(b)]. Further details on device fabrication can be found in the Appendix and in Ref. [12]. The dominant carriers are n -type and the current-voltage relationship is approximately linear at ambient temperatures.

We apply a scanning probe thermometry technique based on scanning thermal microscopy (SThM). As shown in Fig. 1(b), a sinusoidal alternating current with amplitude I and frequency f_{mod} is passed through the device. The device responds thermally with Peltier heating and cooling at $1f_{\text{mod}}$ and Joule heating at $2f_{\text{mod}}$. We denote these temperature responses with $\Delta T_{\text{Peltier}}$ and ΔT_{Joule} , respectively. A silicon SThM probe with integrated resistive sensor is then raster-scanned across the sample. The sensor is thermally coupled to a spot on the sample surface through a sharp tip. The tip radius can be as small as 3 nm [28]. Changes in the sample surface temperature T_{sample} influence the equilibrium temperature of the sensor T_{sensor} , which in turn changes the sensor element’s electrical resistance. The sample topography is measured simultaneously as in standard contact mode atomic force microscopy (AFM).

II. RESULTS AND DISCUSSION

We recorded Joule and Peltier SThM signals of self-heated NW samples with target WZ segment lengths of 40, 80, and 160 nm. Temperature maps were recorded for different modulation current amplitudes I . Exemplary plots of AFM topography, $\Delta T_{\text{Peltier}}$, and ΔT_{Joule} for each device are shown in Fig. 2. From these, line profiles of $\Delta T_{\text{Peltier}}$ along the nanowires were extracted, which are also shown

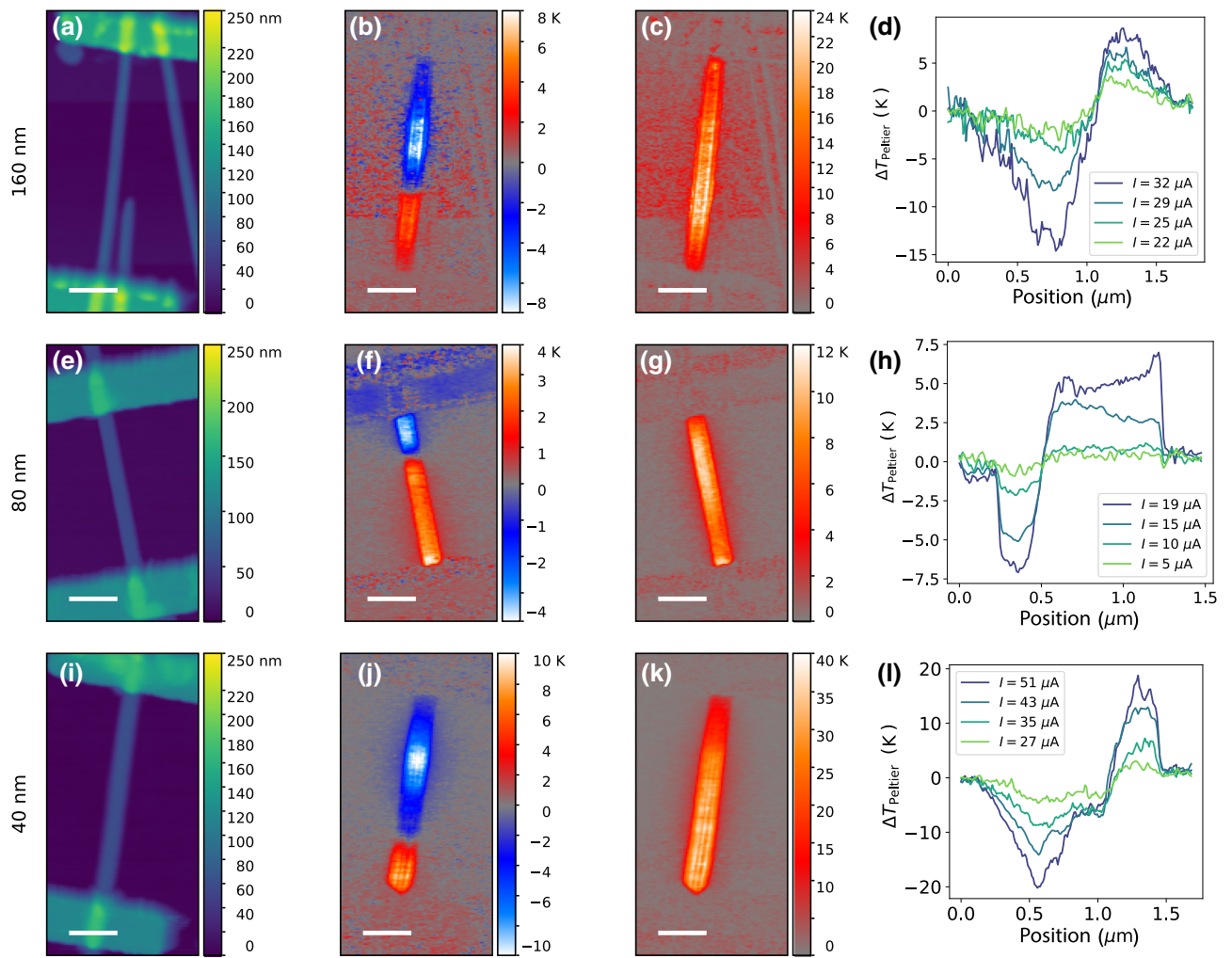


FIG. 2. SThM results for three devices with different targeted WZ segment lengths: (a) AFM topography map for 160 nm, (b) $\Delta T_{\text{Peltier}}$ map for 160 nm, (c) ΔT_{Joule} map for 160 nm, and (d) line profiles of $\Delta T_{\text{Peltier}}$ along the 160 nm nanowire axis for different values of I . The same depictions for (e)–(h) 80 nm and (i)–(l) 40 nm. Shown temperature change maps always correspond to the highest value of I stated in the legend of the associated profile plot. The locations of the barriers are assumed to roughly coincide with the transition between heating and cooling in the $\Delta T_{\text{Peltier}}$ maps. The profiles have an averaging width of five pixels at a square pixel size of 10 nm. For all scans, the horizontal direction as depicted is the fast scanning direction. The display ranges in the temperature maps have been limited to increase the contrast. All scale bars are 300 nm.

in Fig. 2. Profiles for ΔT_{Joule} and data for additional values of I are shown in the Supplemental Material [29]. All three devices show a clear $\Delta T_{\text{Peltier}}$ signal. The position of the WZ segment along the NWs between the electrodes can be identified to be in the region of sign change of the Peltier signal. Let us first discuss the markedly different qualitative behavior of the three devices shown.

For the 160 nm device, the peaks of $\Delta T_{\text{Peltier}}$ are close to the transition between heating and cooling, which is steep with a linear gradient. This is the expected behavior for heating and cooling power that is concentrated close to the crystal phase junctions. This suggests that $\Delta T_{\text{Peltier}}$ is dominated by the barrier Peltier effect. However, the positions of maximum and minimum temperatures are spaced

further apart than the length of the WZ segment. This is an indication that the release of Peltier heat does not occur sharply at the crystal phase junctions, but is spatially distributed away from the junctions into the ZB sections towards the contacts. We analyze this in more detail below. We note that the lateral resolution of SThM is required to reveal these observations.

For the 80 nm device, the profiles look significantly different. Here, $\Delta T_{\text{Peltier}}$ stays more uniform along the ZB sections. For the highest I of 19 μA , we see a peak of $\Delta T_{\text{Peltier}}$ at the bottom contact rather than at the transition between heating and cooling. Unlike the previous example, Peltier heating and cooling is not concentrated around the WZ segment region. In addition, a Peltier effect due to the

metal-NW interface appears to come into play. The signs of the associated Peltier coefficients (or Seebeck coefficients) are opposite for the two effects, such that they add up constructively on either side of the device. We expect that the Seebeck coefficient of an energy barrier is always positive, while the Seebeck coefficient of an InAs NW is negative [30], as also determined by SThM [24,31]. The Seebeck coefficient of the metal electrodes is two orders of magnitude lower and can be neglected [32]. It appears that the barrier effect rolls off for high currents, while the contact effect becomes more dominant. This is manifested in the slope changing from decreasing towards the bottom contact to increasing towards the bottom contact when going from $I_{\text{mod}} = 15 \mu\text{A}$ to $18 \mu\text{A}$ in Fig. 2(h). We acknowledge at this point that the barrier emission effect is inherently nonlinear in nature. We assume that a constant effective Peltier coefficient corresponds to averaging by linearization. We do not observe any signal at odd-order higher harmonics, indicating the absence of significant distortions. We therefore believe that the consequences of this simplification are marginal. The very flat temperature rise observed is remarkable, as it indicates that the heating and cooling power is distributed on a length scale comparable to the system size, which we interpret as a sign of an electron thermalization length on the order of 100 nm. The sharp peak observed at the bottom contact for $I = 19 \mu\text{A}$ might be an artifact of the tip scratching the contact, or it might indicate the existence of a Shottky barrier at the contact.

The data for the 40 nm device show a continuation of the trend. Here, the transition between heating and cooling is not the point of steepest gradient. The temperature profile is almost flat at the transition in the region of the WZ segment. The peaks of $\Delta T_{\text{Peltier}}$ appear to be separated from the barrier region. This indicates that the contact Peltier effect is now dominant compared to the thermionic emission effect. The peaks are however not directly at the contacts and we observe an asymmetric profile, which confirms that the barrier also has an influence in the 40 nm WZ system.

In summary, the first comparison of NWs with different WZ segment lengths suggests the presence of two Peltier effects, one at the energy barrier and one at the NW-metal contacts. The relative weight of the resulting temperature change in the relevant device areas depends on the segment length and potentially also on the applied bias. The first and obvious explanation for this trend is that, for short barrier lengths, the heating and cooling poles are closer to each other. Since the material separating the two poles is in all cases WZ InAs, shorter segments lead to smaller thermal resistances between the two, meaning that the heating and cooling sides can exchange heat more efficiently. Therefore, the barrier Peltier effect has to be less dominant for shorter WZ segments if we assume that the Peltier coefficient is identical for all barrier lengths. However, the shape

of the barrier may be influenced when the WZ segments become shorter. In particular, the barrier could be lowered for shorter segments [12]. The observation made for the 80 nm barrier suggests that the barrier emission effect levels out for large biases, which may be a sign of the onset of electron tunneling at larger biases. The shape of the resulting temperature distribution strongly suggests a spatially distributed Peltier heating and cooling power.

The qualitative discussion above calls for a more quantitative analysis. To this end, we investigate a fourth device, again with a nominal WZ segment length of 80 nm. We perform a scan at a modulation current amplitude of $I = 45 \mu\text{A}$, but this time focusing on maximizing resolution and sensitivity with smaller pixel size and a slower modulation frequency (see the experimental section for details). The result is shown in Fig. 3. Again, the transition between heating and cooling is not centered between the contacts. A line profile for $\Delta T_{\text{Peltier}}$ along the wire is shown in Fig. 4. The exact position of this profile on the temperature map is shown in the Supplemental Material [29].

Considering that phonons are the dominant carriers of heat in InAs NWs, and that the phonon mean free path is limited by the NW diameter [33], a one-dimensional heat diffusion model is justified. Note that the charge carriers have significantly longer equilibration lengths, on the order of hundreds of nanometers, in comparison to phonons limited to the wire diameter. As noted above, the Peltier power is spatially distributed. We therefore introduce a Peltier coefficient per unit length (unit $\text{WA}^{-1}\text{m}^{-1}$) and denote it with π . We then consider the diffusion of heat from Peltier sources and sinks independently from Joule heating (see the Appendix for details). All measurements and modulations are made on time scales much longer than the

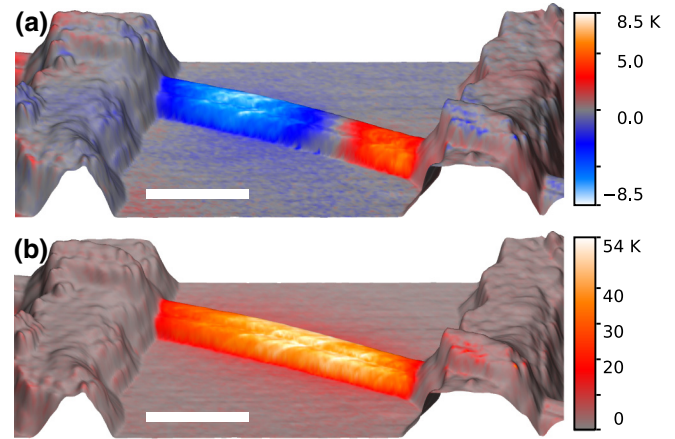


FIG. 3. Data obtained for a fourth device, again with a target WZ segment length of 80 nm. A slower, more detailed scan at $I = 45 \mu\text{A}$ is shown. Shown are three-dimensional (3D) rendered overlay maps of AFM topography with (a) $\Delta T_{\text{Peltier}}$ and (b) ΔT_{Joule} . The fast scanning direction is horizontal. Scale bars are 300 nm.

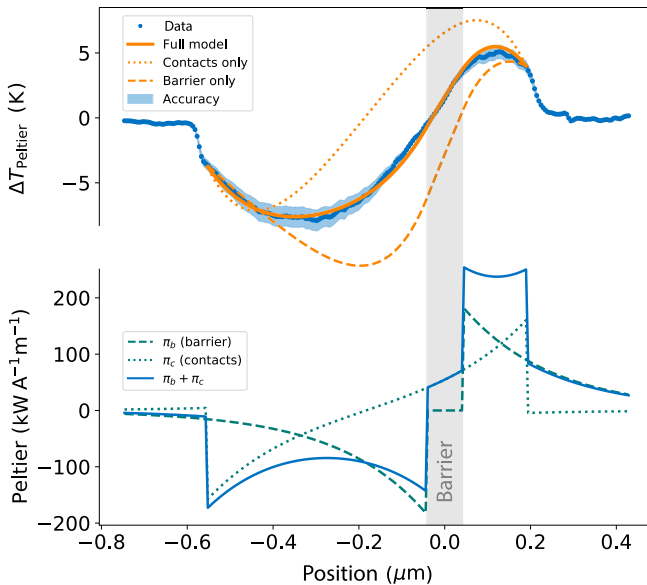


FIG. 4. Top: Line profile of $\Delta T_{\text{Peltier}}$ along the nanowire from Fig. 3. Averaging width of 20 pixels at a pixel size of 2.5 nm. A fit of Eq. (1) is drawn, together with a model that tries to explain all observed Peltier power with only the contact Peltier effect, and a solution which tries to explain all observed Peltier power with only the barrier Peltier effect. The blue shaded area indicates the accuracy limits. See the Supplemental Material [29] for details. Bottom: Electron thermalization model. The Peltier coefficient per unit length is decaying exponentially away from junctions. The electron thermalization length is comparable to the system size.

equilibration time scale of the nanowire system. We can thus apply the steady-state solution of the one-dimensional heat diffusion equation for $\Delta T_{\text{Peltier}}$:

$$\kappa A \frac{\partial^2 \Delta T_{\text{Peltier}}}{\partial x^2}(x) = -\pi(x)I + g\Delta T_{\text{Peltier}}(x). \quad (1)$$

Here the x direction is along the wire axis, κ is the thermal conductivity, A is the cross-sectional area of the wire, $\pi(x)$ is the previously mentioned Peltier coefficient per unit length, and g is the thermal conductance per unit length from the nanowire to underlying substrate. This model predicts $\Delta T_{\text{Peltier}}(x)$, which we compare with an experimental line profile taken from an SThM map of $\Delta T_{\text{Peltier}}$ along the wire.

The physical properties of the system extracted as fit parameters are given in Table I. The model has seven parameters that could be extracted by the fitting. Owing to the high spatial resolution of the experiment, the model has 143 remaining degrees of freedom. While the per-pixel temperature sensitivity of approximately 250 mK (approximately 56 mK for an averaged point on a profile line) is determined by random noise, the accuracy of a given temperature value on the order of 10% is determined by probe

TABLE I. Physical parameters extracted from fit.

Parameter	Value	Unit
x_b	0 ± 3	nm
l_b	84 ± 4	nm
Λ	223 ± 9	nm
κ	8.9 ± 0.5	$\text{W m}^{-1} \text{K}^{-1}$
$\pi_{0,b}$	176 ± 28	$\text{kW A}^{-1} \text{m}^{-1}$
$\pi_{0,c}$	156 ± 22	$\text{kW A}^{-1} \text{m}^{-1}$
g	0.3 ± 0.1	$\text{W m}^{-1} \text{K}^{-1}$

variations, underlying assumptions, and the sensor calibration. The range within the limits of accuracy are drawn in light blue in Fig. 4. A discussion of the uncertainties can be found in the Supplemental Material [29]. See the Appendix for details of the fitting procedure.

A central aspect of this analysis is the shape of $\pi(x)$. As discussed above, we expect a significant distribution of $\pi(x)$. As this distribution originates from the time or distance required for nonequilibrium charge carriers to equilibrate with the lattice through inelastic scattering processes, we expect $\pi(x)$ to have the shape of an exponential decay away from junctions, where contributions from different junctions are added. Simulations of electron-phonon energy exchange at thin energy barriers in a semiconductor material have shown that the power density in fact follows an exponential decay in essence [27], with equal and opposite magnitudes on either side of the barrier. Since we have the same material (ZB InAs) in which charge carriers are injected and extracted at the contacts, it is reasonable to assume the same decay length for the contact Peltier effect. We denote the electron thermalization length with Λ and design a parametrization of $\pi(x)$ around these insights, which is illustrated in the bottom graph of Fig. 4 for the optimal set of parameters found. We note that the description of the source term $\pi(x)$ relates to the electron system only and does not contain contributions from phonons, which enter the thermal conductivity terms. We further note that this description is essentially different from a spatially distributed Seebeck coefficient, which can be related to carrier densities around a p - n junction in semiconductors [34].

Let us discuss the values of the physical parameters we have extracted.

The barrier length (WZ segment length) l_b and the barrier location x_b : In an earlier study, the actual WZ segment length achieved when targeting 80 nm was determined to be statistical with a value of (82 ± 17) nm, which is consistent with the value for l_b that we find here. As expected from the tolerances of the fabrication process, the most plausible location of the barrier is not right in between the contacts, here set to 0.

Thermoelectric properties: The effective Peltier coefficient Π associated with a junction (unit WA^{-1}) can

be found by integration of the relevant component of π . For our exponential decay model, this simply means that $\Pi = \Lambda\pi$. We find a value associated with the barrier of $\Pi_b = (39 \pm 7)$ mV. The Peltier coefficient and the Seebeck coefficient S are fundamentally connected through $S = \Pi/T_{\text{avg}}$. For the average temperature T_{avg} , we take the room temperature plus the average value of ΔT_{Joule} on the wire. We obtain a value for the barrier Seebeck coefficient of $S_b = (89 \pm 21)$ $\mu\text{V/K}^{-1}$.

The value of S depends on the chemical potential of the sample, which in InAs nanowires usually depends on surface charges. The conductance of the wires used here implies an electron concentration in the low 10^{18} cm^{-3} range in the ZB part. This is consistent with observation in the literature. For bulk InAs with an oxidized surface, the surface Fermi level was reported to be pinned approximately 100 meV above the conduction band edge [35,36]. Similarly, for ZB InAs nanowires with diameters smaller than 100 nm, the effective Fermi level was also found to be approximately 100 meV above the conduction band edge in different experiments [12,37]. It is worth noting that background carbon dopant incorporation during nanowire growth can also affect the Fermi level position [38]. For these reasons, we expect the Fermi energy of our nanowires to lie about 100 meV above the conduction band edge of ZB InAs, consistent with the observed conductivity value.

It is interesting to make a comparison of S to a previously measured intrinsic Seebeck coefficient of an InAs nanowire [30], which is about half the magnitude compared to the value we find here. Figure 4 also shows a solution to Eq. (1) in which all heat pumping power is purely due to the contacts, and a solution in which all heat pumping power is purely due to the barrier emission effect. If only the contacts contributed, the profile would be symmetric in between the contacts. If the effect was purely due to the barrier, the asymmetry would be even more pronounced, and the peaks of $\Delta T_{\text{Peltier}}$ would lie closer to the presumed barrier location. The observed behavior can only be explained when taking into account both effects.

The value of the thermal conductivity κ of the InAs nanowire that we find here is consistent with the experimental results: Values for κ of single crystalline InAs nanowires of both the ZB phase and the WZ phase have been determined experimentally to lie in a range of $8 - 10$ $\text{W m}^{-1}\text{K}^{-1}$ at room temperature for similar nanowire diameters [39]. Lower values were reported for wires in which a high defect density was either confirmed [30], or could be expected [33]. For these wires, a value for κ around 3 $\text{W m}^{-1}\text{K}^{-1}$ was measured. We expect our wires to be largely defect-free except for a few twin defects and the intentionally introduced WZ segment [12], and therefore also expected κ to be close to the values determined for single-crystalline samples.

The thermoelectric figure of merit $ZT = S^2 T_{\text{avg}} / (\rho\kappa)$ is often used to evaluate the potential of a thermoelectric system for technical applications [40]. From the device's current-voltage characteristics, we estimate $\rho = (22 \pm 6)$ $\mu\Omega\text{m}$, yielding $ZT = 0.02 \pm 0.01$ for the barrier system.

Thermalization length Λ : The decay length is related to the scattering length of the emitted charge carriers. The value we find is on the same order as values reported for the mean free path defined in the context of charge carrier mobility [26,41,42]. It is however important to note that, although the two quantities are related through a notion of scattering length, there are conceptual differences. Both heat and charge are transported by thermally excited charge carriers. Momentum is relaxed through scattering, leading to dispersion of electrical resistance and energy, leading to thermalization. Different scattering mechanisms lead to different relaxation lengths for momentum and energy flux. For charge transport, we typically distinguish elastic scattering (momentum changes direction, but stays the same in magnitude) and inelastic scattering (energy is exchanged with the lattice). Some scattering mechanisms lead to both energy and momentum relaxations, and result in similar scattering and thermalization lengths. This is the case for electron-phonon scattering (mostly inelastic) dominating in clean InAs bulk at room temperature, and also expected for defect scattering (inelastic) in bulk InAs. In contrast, electron-electron scattering leads to a thermalization length shorter than the momentum relaxation relevant to charge transport, but electron-electron scattering is negligible in this system. Nevertheless, a difference between momentum relaxation length scales may apply here: it has been consistently observed in studies of InAs nanowires that boundary scattering and scattering with surface defects can dominate the scattering of charge carriers. These scattering mechanisms have a strong angle dependence that affects the ratio between momentum and energy relaxations. As a consequence, we expect that the scattering length associated with a Drude model of electrical resistance should be an upper limit of the thermalization length observed here. The observation that the relaxation length values obtained are similar therefore provides useful insight into the scattering in the electronic system.

Substrate coupling g (thermal conductance per unit length between the nanowire and substrate): The thermal conductance between the nanowire and underlying substrate, which is a parameter in our model, is not easy to extract from other experiments [21]. The value we extract is (0.3 ± 0.1) $\text{W m}^{-1}\text{K}^{-1}$. This relates to the area-dependent thermal boundary conductance (with units $\text{WK}^{-1}\text{m}^{-2}$) through division by the contact width. For a given length, this conductance is governed by two thermal resistances in series: the thermal boundary resistance \mathcal{R}_{bnd} between the NW and the substrate material, and the thermal spreading resistance in the substrate,

\mathcal{R}_{spr} . By subtracting the influence of the spreading resistance (details are given in the Supplemental Material [29]), we can calculate the thermal boundary resistance per unit length (units $\text{m}^2\text{K/W}$). This relates to the area-dependent thermal boundary conductance (with units $\text{W K}^{-1}\text{m}^{-2}$) through division by the contact width. We find a value for the interfacial thermal conductance of $G_{\text{bnd}} = (12.6 \pm 1.6) \text{ MW K}^{-1}\text{m}^{-2}$.

As a cross-check, we determine G_{bnd} by using the ΔT_{Joule} map and analyzing a profile line orthogonal to the nanowire axis, which is shown in Fig. 5. The exact location of this profile line on the temperature map is shown in the Supplemental Material [29]. Heat spreading into the substrate is manifested as an exponential decay of ΔT_{Joule} away from the wire axis. The value of ΔT_{Joule} directly next to the wire is not accessible in our measurement because of the tip geometry. See Fig. 5 for an illustration of this issue. We fit an exponential function to the accessible part of the heat spreading and extrapolate the temperature immediately next to the wire. The total thermal boundary conductance can now be estimated from the jump in ΔT_{Joule} to the value we measure on top of the wire, which is visible as a plateau in the temperature profile. (The plateau appears because the temperature within the nanowire does not vary over its cross section, as expected from the large mean free path of phonons.) Assumptions about the interface geometry are needed to extract the thermal boundary

conductance per unit area. The nanowire under investigation has a hexagonal cross section. We denote the edge-to-edge distance with d , the corner-to-corner distance with R , and the edge length with t (see the illustration in Fig. 5). Using t as a lower limit for the interface width, we obtain a value of $G_{\text{bnd}} = (22 \pm 8) \text{ MW K}^{-1}\text{m}^{-2}$. It is however likely that the actual contact area between the wire and substrate is wider than t , for instance, because there exists an underfill originating from the processing (such as electron beam resist residues), illustrated in light red in Fig. 5. As an upper limit of the contact width, we extrapolate the touching point to the corner-to-corner width R instead of the edge width t and end up with a value of $(14 \pm 5) \text{ MW K}^{-1}\text{m}^{-2}$. This latter value is in good agreement with the value obtained from the Peltier fit. That the two different approaches yield similar results is seen as confirmation that the method can in fact be used to extract values for the usually difficult to characterize thermal boundary conductance associated with nanoscale thermal interfaces.

III. CONCLUSION

In conclusion, we observe thermoelectric effects around energy barriers formed by crystal phase engineering in InAs nanowires. Direct imaging of the resulting temperature fields with nanoscale spatial resolution is achieved. We find that the thermoelectric heating and cooling power density is spatially distributed on a length scale comparable to the system size. The high spatial resolution and quantitative nature of the method allow us to compare the measurement data with spatially dependent heat diffusion models. We are able to extract the thermalization length of nonequilibrium charge carriers. Thermal transport parameters, including thermal conductivity and thermal boundary resistance to the substrate, are quantified. For the latter, there exists no other characterization method on this length scale. We show that the approach allows for a complete thermoelectric characterization. A thermoelectric figure of merit of $ZT = 0.02 \pm 0.01$ is calculated from the extracted parameters.

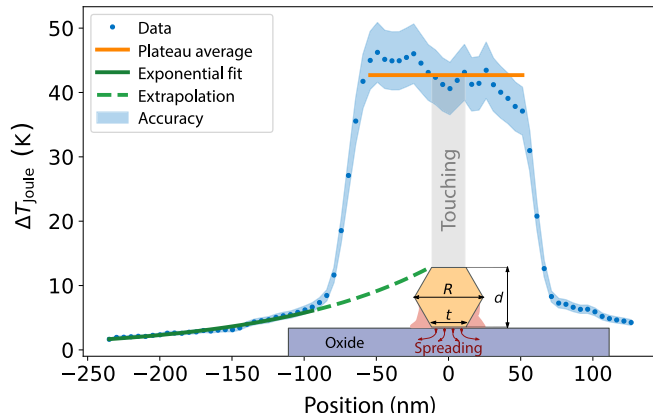


FIG. 5. Joule heating temperature rise profile orthogonal to the wire. An exponential temperature decay away from the wire was fitted to points on the substrate. For geometric reasons, the substrate temperature immediately next to the wire was not accessible in the measurement. The exponential trend was therefore extrapolated to obtain a value for the temperature jump from wire to substrate, from which the boundary resistance was inferred. The comparison with the Peltier profile data showed that the interface width is probably effectively wider than the edge width t , possibly due of the presence of an underfill originating from device processing (illustrated in light red). An illustration of the geometry and heat spreading into the substrate is provided. The blue shaded area indicates the limits of accuracy. See the Supplemental Material [29] for details.

ACKNOWLEDGMENTS

The authors thank U. Drechsler, S. Reidt, and A. Zulji for technical assistance, A. Schenk, K. Moselund, W. Riess, and H. Riel for continuous support, L. Gignac for the TEM image shown in the Supplemental Material [29], and S. Hönl for helping us with 3D rendering. This project has received funding from the European Union's Horizon 2020 research and innovation programme under Grants No. 766853 (EFINED) and No. 767187 (QuIET).

APPENDIX

1. Sample fabrication

The InAs nanowires are grown from Au aerosol seed particles on (111)B InAs substrates by low pressure metal-organic vapor phase epitaxy. The InAs crystal phase is controlled by changing the effective group *V* hydride flow, as described in Refs. [12,15]. Resulting NW diameters are around (60 ± 5) nm. Electron beam lithography is used to define the contact area, which is then etched in a mixture of $(\text{NH}_4)_2\text{S}_x$ and H_2O 1:20 for 1 minute at 40°C . Afterwards, a film of 25 nm Ni and 75 nm Au is evaporated and then lifted off in acetone.

2. Scanning probe thermometry

We again refer to the schematic of the method shown in Fig. 1(b) and provide some more details on the experimental method: A differential electrical signal is created with the help of a Wheatstone bridge circuit. The signal is then amplified and, for each pixel, both time averaged and demodulated at $1f_{\text{mod}}$ and $2f_{\text{mod}}$. The resulting time-averaged signal V_{dc} and the demodulated amplitudes V_{ac} at $1f_{\text{mod}}$ and $2f_{\text{mod}}$ then relate the relevant harmonic content of T_{sample} to the known out-of-contact sensor temperature $\Delta T_{\text{sensor, ooc}}$ through [23,43]

$$\Delta T_{\text{sample}} = \Delta T_{\text{sensor, ooc}} \frac{\Delta V_{\text{ac}}}{\Delta V_{\text{dc}} - \Delta V_{\text{ac}}}, \quad (\text{A1})$$

where ΔV_{dc} is the time-averaged voltage drop over the Wheatstone bridge compared to when the tip is out of contact, and ΔV_{ac} is the demodulated voltage amplitude at the momentarily considered harmonic of f_{mod} . For illustration, the raw signals for the high resolution scan are shown in the Supplemental Material [29]. The sensor is operated in an active mode, meaning that it also serves as a heater that creates a “thermal bias.” The out-of-contact sensor temperature was 274°C as a response to an electrical power dissipation of 1.3 mW in the sensor. We do not expect the heated tip to influence the temperature in the probed region beyond the uncertainties of the method because the tip-sample thermal resistance is large compared to the thermal resistance inside the sample [44]. Experiments are performed in high vacuum (1×10^{-6} mbar) in an electrically and acoustically shielded laboratory with temperature stabilization [45]. As discussed elsewhere [22], we do not expect thermal radiation to play a role in the experiment, even though the structures are of subwavelength size [46]. The dwell time is chosen such that the lock-in can integrate about 20 cycles of the signal. The sensor has a thermal time constant of $38 \mu\text{s}$ [47]. Faster modulation therefore allows for faster scans, but the signals can get attenuated. This attenuation can be corrected when the time constant is known, but it still leads to a lower signal-to-noise ratio [48]. For the low resolution measurements, f_{mod}

was 7234 Hz and, for the high resolution measurements, f_{mod} was 1342 Hz. Additionally, the high resolution scan has a four times smaller pixel size compared to the lower resolution series (2.5 nm vs 10 nm).

3. Modeling methods

The steady-state heat diffusion equation including both Peltier and Joule source terms is

$$\kappa A \frac{\partial^2 \Delta T}{\partial x^2}(x) = -\rho(x)I^2 - \pi(x)I + g\Delta T(x), \quad (\text{A2})$$

where ρ is electrical resistivity. The source term proportional to I^2 is Joule heating and the source term proportional to I captures Peltier and thermoelectric effects.

For the small temperature variations probed here, we may assume that none of the parameters is temperature, current, or voltage dependent. In this case, Eq. (A2) is fully linear and can be decomposed into equations that describe heat conduction for the two source terms individually, in accordance with the thermometry method employed, which can discern between temperature changes induced by Joule and Peltier heat sources and sinks. For the Peltier part, we then obtain Eq. (1).

The properties g , κ , ρ , and A are not expected to vary along the nanowire and are assumed to be independent of x . It has been predicted and experimentally shown [39] that the thermal impedance mismatch between WZ InAs and ZB InAs is small. This is why in the model, κ is assumed to be the same for WZ and ZB. There are however experimental indications that a thermal resistance is associated with an interface between WZ and ZB [30,33]. This interfacial resistance has been estimated and included in the model. See the Supplemental Material [29] for details.

For extracting physical parameters, we solve Eq. (1) numerically with a boundary value solver for ordinary differential equations and perform a weighted nonlinear least square fit of the model parameters [49,50]. A discussion of the uncertainties is provided in the Supplemental Material [29].

-
- [1] Cronin B. Vining, An inconvenient truth about thermoelectrics, *Nat. Mater.* **8**, 83 (2009).
 - [2] Giuliano Benenti, Giulio Casati, Keiji Saito, and Robert S. Whitney, Fundamental aspects of steady-state conversion of heat to work at the nanoscale, *Phys. Rep.* **694**, 1 (2017).
 - [3] K. Horio and H. Yanai, Numerical modeling of heterojunctions including the thermionic emission mechanism at the heterojunction interface, *IEEE Trans. Electron Devices* **37**, 1093 (1990).
 - [4] Ali Shakouri and John E. Bowers, Heterostructure integrated thermionic coolers, *Appl. Phys. Lett.* **71**, 1234 (1997).

- [5] A. Shakouri, E. Y. Lee, D. L. Smith, V. Narayananmurti, J. E. Bowers, and J. E. Bowers, Thermoelectric effects in submicron heterostructure barriers, *Microscale Thermophys. Eng.* **2**, 37 (1998).
- [6] Kyoungsoon Yang, Jack R. East, and George I. Hadad, Numerical modeling of abrupt heterojunctions using a thermionic-field emission boundary condition, *Solid State Electron.* **36**, 321 (1993).
- [7] P. Caroff, K. A. Dick, J. Johansson, M. E. Messing, K. Deppert, and L. Samuelson, Controlled polytypic and twin-plane superlattices in III–V nanowires, *Nat. Nanotechnol.* **4**, 50 (2009).
- [8] Kimberly A. Dick, Philippe Caroff, Jessica Bolinsson, Maria E. Messing, Jonas Johansson, Knut Deppert, L. Reine Wallenberg, and Lars Samuelson, Control of III–V nanowire crystal structure by growth parameter tuning, *Semicond. Sci. Technol.* **25**, 024009 (2010).
- [9] Sebastian Lehmann, Jesper Wallentin, Daniel Jacobsson, Knut Deppert, and Kimberly A. Dick, A general approach for sharp crystal phase switching in InAs, GaAs, InP, and GaP nanowires using only group V flow, *Nano Lett.* **13**, 4099 (2013).
- [10] Dong Pan, Mengqi Fu, Xuezhe Yu, Xiaolei Wang, Lijun Zhu, Shuaihua Nie, Siliang Wang, Qing Chen, Peng Xiong, Stephan von Molnár, and Jianhua Zhao, Controlled synthesis of phase-pure InAs nanowires on Si(111) by diminishing the diameter to 10 nm, *Nano Lett.* **14**, 1214 (2014).
- [11] Abderrezak Belabbes, Christian Panse, Jürgen Furthmüller, and Friedhelm Bechstedt, Electronic bands of III–V semiconductor polytypes and their alignment, *Phys. Rev. B* **86**, 075208 (2012).
- [12] I-Ju Chen, Sebastian Lehmann, Malin Nilsson, Pyry Kivilahti, Heiner Linke, Kimberly A. Dick, and Claes Thelander, Conduction band offset and polarization effects in InAs nanowire polytype junctions, *Nano Lett.* **17**, 902 (2017).
- [13] N. Akopian, G. Patriarche, L. Liu, J.-C. Harmand, and V. Zwiller, Crystal phase quantum dots, *Nano Lett.* **10**, 1198 (2010).
- [14] Malin Nilsson, I-Ju Chen, Sebastian Lehmann, Vendula Mauerova, Kimberly A. Dick, and Claes Thelander, Parallel-coupled quantum dots in InAs nanowires, *Nano Lett.* **17**, 7847 (2017).
- [15] Malin Nilsson, Luna Namazi, Sebastian Lehmann, Martin Leijnse, Kimberly A. Dick, and Claes Thelander, Single-electron transport in InAs nanowire quantum dots formed by crystal phase engineering, *Phys. Rev. B* **93**, 195422 (2016).
- [16] Ming Wang, Chong Bi, Ling Li, Shbing Long, Qi Liu, Hangbing Lv, Nianduan Lu, Pengxiao Sun, and Ming Liu, Thermoelectric Seebeck effect in oxide-based resistive switching memory, *Nat. Commun.* **5**, 4598 (2014).
- [17] Eilam Yalon, Sanchit Deshmukh, Miguel Muñoz Rojo, Feifei Lian, Christopher M. Neumann, Feng Xiong, and Eric Pop, Spatially resolved thermometry of resistive memory devices, *Sci. Rep.* **7**, 15360 (2017).
- [18] Jaeho Lee, Mehdi Asheghi, and Kenneth E. Goodson, Impact of thermoelectric phenomena on phase-change memory performance metrics and scaling, *Nanotechnology* **23**, 205201 (2012).
- [19] Dong-Seok Suh, Cheolkyu Kim, Kijoon H. P. Kim, Youn-Seon Kang, Tae-Yon Lee, Yoonho Khang, Tae Sang Park, Young-Gui Yoon, Jino Im, and Jisoon Ihm, Thermoelectric heating of Ge₂Sb₂Te₅ in phase change memory devices, *Appl. Phys. Lett.* **96**, 123115 (2010).
- [20] Eric Pop, Energy dissipation and transport in nanoscale devices, *Nano Res.* **3**, 147 (2010).
- [21] David G. Cahill, Wayne K. Ford, Kenneth E. Goodson, Gerald D. Mahan, Arun Majumdar, Humphrey J. Maris, Roberto Merlin, and Simon R. Phillpot, Nanoscale thermal transport, *J. Appl. Phys.* **93**, 793 (2002).
- [22] Fabian Könemann, Morten Vollmann, Tino Wagner, Norizawati Mohd Ghazali, Tomohiro Yamaguchi, Andreas Stemmer, Koji Ishibashi, and Bernd Gotsmann, Thermal conductivity of a supported multiwalled carbon nanotube, *J. Phys. Chem. C* **123**, 12460 (2019).
- [23] F. Könemann, M. Vollmann, F. Menges, I. Chen, N. M. Ghazali, T. Yamaguchi, K. Ishibashi, C. Thelander, and B. Gotsmann, in *2018 24rd International Workshop on Thermal Investigations of ICs and Systems (THERMINIC)*, (IEEE, Stockholm, Sweden, 2018), p. 1.
- [24] Fabian Menges, Philipp Mensch, Heinz Schmid, Heike Riel, Andreas Stemmer, and Bernd Gotsmann, Temperature mapping of operating nanoscale devices by scanning probe thermometry, *Nat. Commun.* **7**, 10874 (2016).
- [25] Achim Harzheim, Jean Spiece, Charalambos Evangelis, Edward McCann, Vladimir Falko, Yuewen Sheng, Jamie H. Warner, G. Andrew D. Briggs, Jan A. Mol, Pascal Gehring, and Oleg V. Kolosov, Geometrically enhanced thermoelectric effects in graphene nanoconstrictions, *Nano Lett.* **18**, 7719 (2018).
- [26] I-Ju Chen, Adam Burke, Artis Svilans, Heiner Linke, and Claes Thelander, Thermoelectric Power Factor Limit of a 1d Nanowire, *Phys. Rev. Lett.* **120**, 177703 (2018).
- [27] Roger Lake and Supriyo Datta, Energy balance and heat exchange in mesoscopic systems, *Phys. Rev. B* **46**, 4757 (1992).
- [28] Yu Kyoung Ryu Cho, Colin D. Rawlings, Heiko Wolf, Martin Spieser, Samuel Bisig, Steffen Reidt, Marilynne Sousa, Subarna R. Khanal, Tevis D. B. Jacobs, and Armin W. Knoll, Sub-10 nanometer feature size in silicon using thermal scanning probe lithography, *ACS Nano* **11**, 11890 (2017).
- [29] See Supplemental Material at <http://link.aps.org/supplemental/10.1103/PhysRevApplied.13.054035> for Peltier and Joule temperature change maps for all measured excitation amplitudes of the low-resolution series, estimation of WZ/ZB boundary resistance, raw data and 2D result plots with drawn profile lines for the high resolution measurement, discussion of uncertainties for the temperature profile analysis.
- [30] S. F. Karg, V. Troncale, U. Drechsler, P. Mensch, P. Das Kanungo, H. Schmid, V. Schmidt, L. Gignac, H. Riel, and B. Gotsmann, Full thermoelectric characterization of InAs nanowires using MEMS heater/sensors, *Nanotechnology* **25**, 305702 (2014).
- [31] F. Menges, F. Motzfeld, H. Schmid, P. Mensch, M. Dittberner, S. Karg, H. Riel, and B. Gotsmann, in *2016 IEEE*

- International Electron Devices Meeting (IEDM)* (IEEE, San Francisco, USA, 2016), p. 15.8.1.
- [32] Aldo Vieira Da Rosa, *Fundamentals of Renewable Energy Processes* (Academic Press, Cambridge Massachusetts, 2012). Google-Books-ID: 7LX3yrVEgCMC.
- [33] M. Y. Swinkels, M. R. van Delft, D. S. Oliveira, A. Cavalli, I. Zardo, R. W. van der Heijden, and E. P. A. M. Bakkers, Diameter dependence of the thermal conductivity of InAs nanowires, *Nanotechnology* **26**, 385401 (2015).
- [34] H.-K. Lyeo, A. A. Khajetoorians, L. Shi, K. P. Pipe, R. J. Ram, A. Shakouri, and C. K. Shih, Profiling the thermoelectric power of semiconductor junctions with nanometer resolution, *Science* **303**, 816 (2004).
- [35] H.-U. Baier, L. Koenders, and W. Mönch, Oxidation of cleaved InAs (1 1 0) surfaces at room temperature: Surface band-bending and ionization energy, *Solid State Commun.* **58**, 327 (1986).
- [36] D. C. Tsui, Observation of Surface Bound State and Two-Dimensional Energy Band by Electron Tunneling, *Phys. Rev. Lett.* **24**, 303 (1970).
- [37] Volker Schmidt, Philipp F. J. Mensch, Siegfried F. Karg, Bernd Gotsmann, Pratyush Das Kanungo, Heinz Schmid, and Heike Riel, Using the Seebeck coefficient to determine charge carrier concentration, mobility, and relaxation time in InAs nanowires, *Appl. Phys. Lett.* **104**, 012113 (2014).
- [38] Claes Thelander, Kimberley A. Dick, M. T. Borgström, Linus E. Fröberg, Philippe Caroff, H. A. Nilsson, and Lars Samuelson, The electrical and structural properties of n-type inas nanowires grown from metal–organic precursors, *Nanotechnology* **21**, 205703 (2010).
- [39] Feng Zhou, Arden L. Moore, Jessica Bolinsson, Ann Persson, Linus Fröberg, Michael T. Pettes, Huijun Kong, Lew Rabenberg, Philippe Caroff, Derek A. Stewart, Natalio Mingo, Kimberley A. Dick, Lars Samuelson, Heiner Linke, and Li Shi, Thermal conductivity of indium arsenide nanowires with wurtzite and zinc blende phases, *Phys. Rev. B* **83**, 205416 (2011).
- [40] G. Jeffrey Snyder and Eric S. Toberer, in *Materials for Sustainable Energy* (Co-Published with Macmillan Publishers Ltd, UK, 2010), p. 101.
- [41] Steven Chuang, Qun Gao, Rehan Kapadia, Alexandra C. Ford, Jing Guo, and Ali Javey, Ballistic InAs nanowire transistors, *Nano Lett.* **13**, 555 (2013).
- [42] X. Zhou, S. A. Dayeh, D. Aplin, D. Wang, and E. T. Yu, Scanned electrical probe characterization of carrier transport behavior in InAs nanowires, *J. Vac. Sci. Technol. B: Microelectron. Nanometer Struct. Process., Meas., Phenom.* **24**, 2036 (2006).
- [43] Fabian Menges, Heike Riel, Andreas Stemmer, and Bernd Gotsmann, Nanoscale thermometry by scanning thermal microscopy, *Rev. Sci. Instrum.* **87**, 074902 (2016).
- [44] Fabian Menges, Heike Riel, Andreas Stemmer, and Bernd Gotsmann, Quantitative thermometry of nanoscale hot spots, *Nano Lett.* **12**, 596 (2012).
- [45] Emanuel Lötscher, Daniel Widmer, and Bernd Gotsmann, Next-generation nanotechnology laboratories with simultaneous reduction of all relevant disturbances, *Nanoscale* **5**, 10542 (2013).
- [46] Sheng Shen, Arvind Narayanaswamy, and Gang Chen, Surface phonon polaritons mediated energy transfer between nanoscale gaps, *Nano Lett.* **9**, 2909 (2009).
- [47] U. Dürig, Fundamentals of micromechanical thermoelectric sensors, *J. Appl. Phys.* **98**, 044906 (2005).
- [48] A. Majumdar, Scanning thermal microscopy, *Annu. Rev. Mater. Sci.* **29**, 505 (1999).
- [49] T. E. Oliphant, Python for scientific computing, *Comput. Sci. Eng.* **9**, 10 (2007).
- [50] Tilo Strutz, *Data Fitting and Uncertainty: A Practical Introduction to Weighted Least Squares and beyond* (Springer Vieweg, Wiesbaden, Germany, 2016), 2nd ed.